BAMS Article

Introducing the New Regional Community Earth System Model, R-CESM

Dan Fu, Justin Small, Jaison Kurian, Yun Liu, Brian Kauffman, Abishek Gopal, Sanjiv Ramachandran, Zhi Shang, Ping Chang, Gokhan Danabasoglu, Katherine Thayer-Calder, Mariana Vertenstein, Xiaohui Ma, Hengkai Yao, Mingkui Li, Zhao Xu, Xiaopei Lin, Shaoqing Zhang, and Lixin Wu

ABSTRACT: The development of high-resolution, fully coupled, regional Earth system model systems is important for improving our understanding of climate variability, future projections, and extreme events at regional scales. Here we introduce and present an overview of the newly developed Regional Community Earth System Model (R-CESM). Different from other existing regional climate models, R-CESM is based on the Community Earth System Model version 2 (CESM2) framework. We have incorporated the Weather Research and Forecasting (WRF) Model and Regional Ocean Modeling System (ROMS) into CESM2 as additional components. As such, R-CESM can be conveniently used as a regional dynamical downscaling tool for the global CESM solutions or/and as a standalone high-resolution regional coupled model. The user interface of R-CESM follows that of CESM, making it readily accessible to the broader community. Among countless potential applications of R-CESM, we showcase here a few preliminary studies that illustrate its novel aspects and value. These include 1) assessing the skill of R-CESM in a multiyear, high-resolution, regional coupled simulation of the Gulf of Mexico; 2) examining the impact of WRF and CESM ocean–atmosphere coupling physics on tropical cyclone simulations; and 3) a convection-permitting simulation of submesoscale ocean–atmosphere interactions. We also discuss capabilities under development such as (i) regional refinement using a high-resolution ROMS nested within global CESM and (ii) "online" coupled data assimilation. Our open-source framework (publicly available at https://github.com/ihesp/rcesm1) can be easily adapted to a broad range of applications that are of interest to the users of CESM, WRF, and ROMS.

KEYWORDS: Climate models; Coupled models; Regional models

https://doi.org/10.1175/BAMS-D-20-0024.1
Corresponding author: Justin Small, jsmall@ucar.edu
In final form 10 May 2021
©2021 American Meteorological Society
For information regarding reuse of this content and general copyright information, consult the AMS Copyright Policy.

Unauthenticated | Downloaded 08/28/24 03:34 AM UTC

AFFILIATIONS: Fu, Kurian, Liu, Gopal, and Ramachandran—International Laboratory for High-Resolution Earth System Prediction, and Department of Oceanography, Texas A&M University, College Station, Texas; **Small, Kauffman, and Danabasoglu**—International Laboratory for High-Resolution Earth System Prediction, and National Center for Atmospheric Research, Boulder, Colorado; **Shang**—Department of Oceanography, Texas A&M University, College Station, Texas; **Chang**—International Laboratory for High-Resolution Earth System Prediction, and Department of Oceanography, and Department of Atmospheric Sciences, Texas A&M University, College Station, Texas; **Thayer-Calder and Vertenstein**—National Center for Atmospheric Research, Boulder, Colorado; **Ma, Li, and Zhang**—International Laboratory for High-Resolution Earth System Prediction, Texas A&M University, College Station, Texas, and Key Laboratory of Physical Oceanography/Frontiers Science Center for Deep Ocean Multispheres and Earth System, Ocean University of China, and Laboratory for Ocean Dynamics and Climate, Qingdao Pilot National Laboratory for Marine Science and Technology, Qingdao, China; **Yao**—Department of Oceanography, Texas A&M University, College Station, Texas, and Key Laboratory of Physical Oceanography/Frontiers Science Center for Deep Ocean Multispheres and Earth System, Ocean University of China, Qingdao, China; **Xu, Lin, and Wu**—Key Laboratory of Physical Oceanography/Frontiers Science Center for Deep Ocean Multispheres and Earth System, Ocean University of China, and Laboratory for Ocean Dynamics and Climate, Qingdao Pilot National Laboratory for Marine Science and Technology, Qingdao, China

Earth system models (ESMs), in which different components such as atmosphere, land, ocean, sea ice, biogeochemistry, and river runoff interact with each other, are the most comprehensive tools to understand and predict the Earth's weather (minutes to days) and climate (seasons to centuries) systems. Due to computational costs, current global ESMs are often configured with coarse horizontal resolutions but usually have multiple ensemble members, and are typically designed to study climatic evolution (e.g., Kay et al. 2015). In contrast, regional ESMs are configured with much higher resolution and dedicated to either weather applications or high-resolution dynamical downscaling of climate information from coarse-resolution global models, and most do not contain active ocean components (e.g., Giorgi 2019; Gutowski et al. 2020). The global and regional ESMs differ in many other aspects, including available component models, resolved and parameterized physics, and model framework. Given the ever-increasing demand for high-resolution regional weather and climate information for decision and policy making, it is desirable to have a system where one can switch seamlessly from global to regional and weather to climate applications. This is the primary motivation for us to develop and introduce the Regional Community Earth System Model (R-CESM).

Existing approaches to bridge the gap between global and regional ESMs involve methods such as running global models at a uniform high-resolution, regional mesh refinement, and downscaling from global to regional ESMs. Advances in supercomputing have made it possible to run global models on grids that permit tropical cyclones (TCs) and ocean eddies for long climate time scales (e.g., Kirtman et al. 2012; Delworth et al. 2012; Small et al. 2014; Chang et al. 2020; Roberts et al. 2020). However, these simulations are so far somewhat rare and very computationally expensive, and the grid resolutions may still be insufficient to fully resolve the gridscale forcing and processes (e.g., complex topography and bathymetry) and dynamical evolutions at regional scales. Mesh refinement (where the spatial resolution can be made higher over an area of interest) is a relatively new technique available only in a few models. The most common method is downscaling the global model results with regional models, which is the approach taken here. However, we have identified at least four aspects that are needed in an advanced regional modeling system which are not addressed in existing systems:

Unauthenticated | Downloaded 08/28/24 03:34 AM UTC

1) Model physics consistency: The schemes and formulations used to parameterize physical processes (e.g., air–sea fluxes, planetary boundary layer, cloud microphysics, and convection) are different between the global and regional models.
2) Modeling framework: The absence of community-based coupling software in some models makes it difficult to add new component models. In some cases, there is an air–sea flux consistency issue because the component models compute fluxes independently instead of using a common flux field computed either in a coupler or any of the individual component models.
3) Two-way interaction: Typically, the global models influence the regional models through lateral boundary conditions (one-way), without any feedback from the regional models to the global models.
4) Coupled data assimilation: Data assimilation capacities inherited from uncoupled systems cannot directly fit in a coupled system; the lack of coupled data assimilation system tends to degrade the prediction ability of a regional ESM forecast system.

To advance ESMs and help overcome these issues, R-CESM has been developed jointly by the Texas A&M University (TAMU), the National Center for Atmospheric Research (NCAR), and the Ocean University of China (OUC). R-CESM is based on the latest infrastructure of the Community Earth System Model version 2 (CESM2; Danabasoglu et al. 2020) and its Common Infrastructure for Modeling the Earth (CIME) framework. Furthermore, R-CESM includes non-standard CESM2 components, i.e., the Regional Ocean Modeling System (ROMS; Haidvogel et al. 2008; Shchepetkin and McWilliams 2005) for the ocean and the Weather Research and Forecasting Model (WRF; Skamarock et al. 2008) for the atmosphere. The CIME infrastructure allows users to swap with ease between the global model (CESM2) and regional models.

The main scope of this paper is to introduce this newly developed R-CESM to the research community and showcase its versatility in studying various Earth systems across different temporal and spatial scales. We start with an overview of the system in the next section. The "R-CESM special features" section highlights particular features of R-CESM that distinguish it from other regional systems. The "R-CESM applications" section describes illustrative simulations of the broad range of applications, including a 9-yr simulation of regional climate in the Gulf of Mexico to examine long-term stability of the R-CESM, TC simulations with different air–sea flux parameterizations, and a high-resolution simulation to explore submesoscale air–sea interactions in the Kuroshio Extension. Then we describe two ongoing efforts: (i) embedding of ROMS within CESM to facilitate the communication between regional and global models, and (ii) development of an "online" coupled data assimilation capability within R-CESM for regional climate predictions. This is followed by a summary in the final section.

R-CESM system overview

In this section, the main R-CESM framework is introduced. More details on key features will be given in the "R-CESM special features" section, and details of the configurations of R-CESM component models and model experiments are given in appendix A.

The parent system CESM2. The CESM2 system, which the R-CESM is based on, has seven global prognostic component models for ocean, atmosphere, land, sea ice, land ice, waves, and river runoff (Danabasoglu et al. 2020). These prognostic components can be swapped for their data versions to run a certain model component subject to specified forcings, e.g., an atmosphere-only simulation forced by the observed ocean state. In CESM2, the component models communicate using the coupler component provided by CIME infrastructure (Danabasoglu et al. 2020; see also section "CIME" for more details).

Unauthenticated | Downloaded 08/28/24 03:34 AM UTC

The CESM surface flux formulas and algorithms were originally designed for long climate simulations to study large-scale and usually low-frequency climate dynamics [e.g., climate variability and climate change applications (Gent et al. 2011; Hurrell et al. 2013; Kay et al. 2015; Danabasoglu et al. 2020) and paleo-climate applications (Otto-Bliesner et al. 2016)] on coarse grids (~1° horizontal resolution), with the aim of conserving properties such as heat and freshwater over climate time scales (Bryan et al. 1996). As such, less emphasis was placed on representation of extremes and synoptic events. It is not yet known whether the current CESM surface flux scheme is adequate and effective in simulating extreme events at high resolution, and the R-CESM approach provides an effective way to investigate this problem as will be shown below.

Adding WRF and ROMS to CESM. When using CESM2 in a typical configuration, all the component models are global. The R-CESM approach adds two regional component models to the CESM2/CIME framework: WRF for the atmosphere and ROMS for the ocean. In the R-CESM implementation, WRF, ROMS, and CLM4 (Community Land model, version 4; Lawrence et al. 2019) are coupled using the CIME implemented coupler (other CESM2 components are planned to be incorporated in the future). As is standard in the CESM2/CIME framework, surface fluxes over land are calculated by the land component model (CLM4) and passed to WRF through the coupler. Over the oceans, however, R-CESM can either calculate surface fluxes using the standard flux scheme in CESM2/CIME or employ WRF's built-in surface layer schemes which are communicated to ROMS through the coupler (Fig. 1a). Thus, in R-CESM, users have the flexibility to use air–sea flux calculation schemes of their choice while keeping other model physics the same.

The major changes made to the original ROMS and WRF source codes are the addition of a wrapper code that allows them to interface with the CESM2/CIME framework. For ROMS, these include (i) bypassing surface forcing inputs and surface air–sea flux calculations within ROMS, (ii) sending sea surface temperature (SST) and surface current velocities through the coupler, and (iii) receiving surface fluxes and surface pressure from the coupler. When using the CESM flux scheme to calculate air–sea fluxes, the changes in WRF source code include (i) bypassing surface layer scheme within WRF; (ii) sending temperature, humidity, winds (on the lowest model level), surface downward radiative fluxes, and surface pressure to the coupler; and (iii) receiving turbulent fluxes and stability parameters from the coupler.

As some of the variables required by the WRF planetary boundary layer parameterization schemes were not diagnosed and readily available in the CESM flux scheme (e.g., bulk Richardson number and momentum roughness length), the coupler source code is modified to enable these outputs (see appendix B for details). As such, the CESM flux scheme can be paired with the WRF built-in planetary boundary layer scheme. Similar modifications are incorporated in the atmosphere–land flux calculations in CLM4 to get the required variables for the WRF physics parameterization schemes.

In summary, the key aspects of the R-CESM air–sea flux schemes are

1) consistent surface flux calculations for both ocean and atmospheric components, irrespective of air–sea flux scheme choices (WRF or CESM scheme), and
2) availability of the CESM air–sea flux scheme in WRF, making R-CESM an ideal testbed to validate and tune CESM atmosphere physics parameterizations at very high resolutions.

R-CESM special features. Several existing regional coupled modeling systems use WRF and ROMS (or alternative regional-specific models) as their atmosphere and ocean components. They were developed with particular applications in mind: for example, nearshore regions including surface waves and sediment transport (Warner et al. 2010), TCs (e.g., Chen et al. 2010;

Unauthenticated | Downloaded 08/28/24 03:34 AM UTC

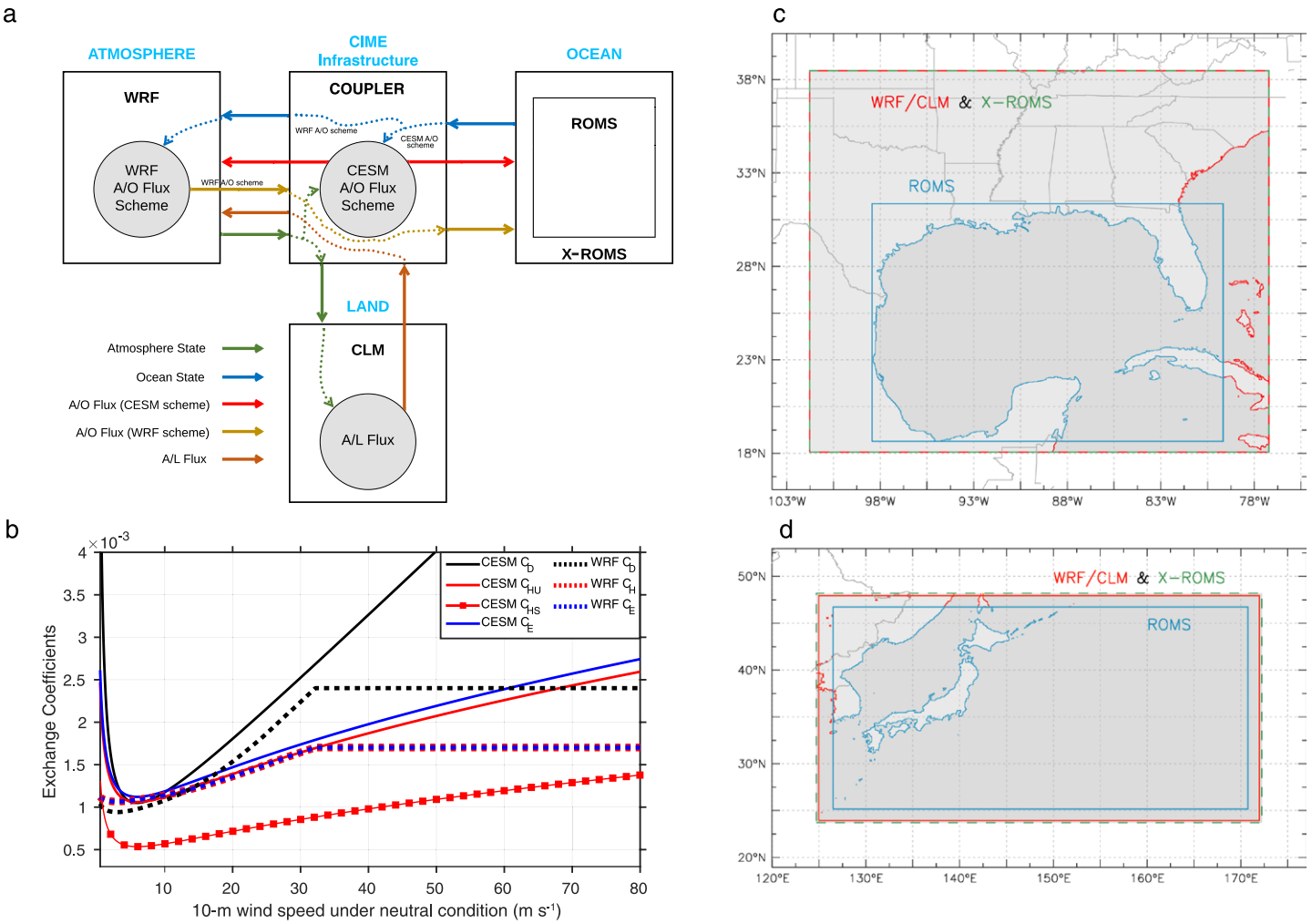

Fig. 1. (a) Schematic of the R-CESM framework, CIME infrastructure, component models, and structure of surface flux calculation. For the CESM flux scheme, atmosphere–ocean (A/O) fluxes are computed by the CIME coupling infrastructure and are then sent to WRF and ROMS (red arrows). For the WRF flux scheme, A/O fluxes are directly computed in WRF, and then transmitted to ROMS through CIME (yellow arrows). Atmosphere–land (A/L) fluxes are always computed in CLM. Here the "atmosphere state" includes temperature, humidity, wind components, surface radiative fluxes, and surface pressure; "ocean state" includes SST and ocean surface current. The A/O and A/L fluxes include momentum, heat, and moisture fluxes as well as some additional variables needed by the WRF boundary layer scheme (e.g., stability functions) and some diagnostic variables (e.g., 2-m air temperature, 10-m wind). (b) Comparison of neutral stability exchange coefficients for drag (C_D), sensible heat (C_H), and latent heat (C_E) as a function of 10-m wind speed using the two surface flux schemes. For CESM flux scheme, C_{HU} and C_{HS} indicate the sensible heat exchange coefficients in unstable and stable atmospheric stability, respectively. We especially note that, for clarity purposes, we only show the WRF MM5 surface scheme with Donelan drag coefficient formulation and constant heat and moisture roughness length (Green and Zhang 2013). CESM flux scheme exchange coefficients are following Fig. 1 of Large and Yeager (2004). R-CESM model domains for (c) the Gulf of Mexico and (d) the Kuroshio Extension simulations presented in this paper. X-ROMS helps ROMS to cover the same region as that of atmosphere and land to facilitate air–sea coupling [see section "POP2 (used in E-CESM)" in appendix A for details].

Smith et al. 2013), regional climate variability (e.g., Xie et al. 2007; Seo et al. 2007; Ma et al. 2016), tropical and boundary ocean current studies (e.g., Samson et al. 2017; Renault et al. 2019), and Arctic simulations (e.g., Maslowski et al. 2012; Cassano et al. 2017). In this paper we do not make detailed comparisons with other particular systems; instead, we highlight notable and unique aspects of R-CESM which should make it better suited for bridging the weather–climate gap—the key objective of R-CESM.

CIME. R-CESM is built upon the CESM2/CIME infrastructure. This infrastructure includes the support scripts (configure, build, run, test), a coupler component, data models, essential

Unauthenticated | Downloaded 09/28/24 03:34 AM UTC

utility external libraries, and other tools required to build a single-executable ESM. CIME uses a flexible hub-and-spoke intercomponent coupling architecture with CIME's coupler component at the hub to which other component models are connected (Fig. 1 of Danabasoglu et al. 2020).

The CIME coupler functionality includes computation of air–sea surface fluxes. CIME also includes tools for generating user-defined mapping weight files that enable regridding between various resolutions in different component models. As such, R-CESM model domain geographic coverage and resolution settings are very flexible, potentially ranging from hundreds of meters to tens of kilometers at any geographic locations depending on user's research focuses. In addition, R-CESM adds the functionality of using active regional models within the CIME's global data models and allows coupling between regional and global component models. Some applications include (i) the Community Atmosphere Model version 6 (CAM6) can be coupled to ROMS in a user-specified region while data ocean model provides observed SST elsewhere, (ii) the Parallel Ocean Program version 2 (POP2) can be coupled to WRF in a regional domain while data atmosphere model provides observation-based atmospheric surface variables elsewhere of the globe, or (iii) using a slab-ocean component model coupled to WRF in a data atmosphere. This broad versatility further distinguishes R-CESM from other existing regional ESMs.

WRF and CESM air–sea flux schemes options. The R-CESM framework offers the unique opportunity to use WRF or CESM air–sea flux schemes and make a thorough comparison between them in an air–sea coupled modeling configuration. A comparison of the fundamental differences between the WRF and CESM air–sea flux schemes used in R-CESM is given in appendix B, and the resulting forms of the exchange coefficients for momentum (i.e., drag coefficient), heat, and moisture are illustrated in Fig. 1b. Notable differences in drag coefficients occur at very low and very high wind speeds. We focus our attention on the high-wind-speed regime due to our topics of interest here, although differences at low wind speeds may also be important. At high wind speeds, the drag coefficient in the CESM scheme increases monotonically while it is capped in the WRF scheme. It has been described by several authors that the drag coefficient for momentum levels off at high wind speeds, e.g., over 30 m s^{-1} (e.g., Donelan et al. 2004; Sanford et al. 2007; Richter et al. 2016; Curcic and Haus 2020), although field measurements at such high wind speeds, as in TCs, are still scarce.

For CESM air–sea flux scheme, Large and Yeager (2009) suggested a high-wind-speed form of the drag coefficient, but so far this has not been implemented in CESM2, partly due to the lack of high-wind-speed events in typical-resolution climate models, and partly due to the continuing uncertainty about the true form of the drag coefficient, i.e., the lack of observations, at such wind speeds.

In addition to uncertainty in the drag coefficient, the enthalpy exchange coefficients are not well known at high wind speeds. The standard CESM scheme shows these coefficients increasing linearly with surface wind speed (Fig. 1b), but recent field experiments have suggested there is no significant wind speed dependence of these coefficients in the hurricane boundary layer (Zhang et al. 2008; Haus et al. 2010; Bell et al. 2012), as suggested in the WRF scheme (Fig. 1b). However, large scatter exists in these observational datasets. R-CESM offers an ideal opportunity to examine the sensitivity of the TC evolution to different formulations of exchange coefficients, thus extending the results of Green and Zhang (2013) using a coupled model.

Advances in supercomputing have made high-resolution CESM simulations more widely used in the area of TC seasonal predictability and future projection studies (e.g., Bacmeister et al. 2014; Wehner et al. 2014; Small et al. 2014; Reed et al. 2015; Zarzycki et al. 2016; Li and Sriver 2018; Roberts et al. 2020; Chang et al. 2020). A natural question to ask is if, or to what extent, the current CESM flux scheme impacts the TC simulation

Unauthenticated | Downloaded 08/28/24 03:34 AM UTC

(in addition to any differences due to dynamical core or parameterizations). The R-CESM approach can readily address this question as shown in the TC hindcast experiments in the "Comparisons of air–sea flux schemes in tropical cyclones simulation" section.

CLM4. CLM4 (Lawrence et al. 2011) is the standard land component in the R-CESM system and it is coupled to WRF through CIME. In the current model configuration, CLM4 has the same horizontal resolution as WRF and it employs nested hierarchical levels to represent land surface heterogeneity. For the first hierarchy, each grid cell consists of up to five subgrid "land units": urban, vegetated, wetland, glacier, and lake. These land units within a single grid cell are driven by the same atmospheric forcing at the reference height. CLM4 contains sophisticated treatment of biogeophysics, hydrology, biogeochemistry, land use, and dynamic vegetation, and has options to describe dynamic vegetation processes responding to varying climate forcings as well as agricultural and urban environments.

Although CLM4 has been internally available as an independent land surface package in WRF since version 3.5, it has reduced functionality compared to the full CLM4 used in R-CESM in some major aspects as detailed in section "CLM4" in appendix A.

In summary, although several regional coupled models have been developed by the community, the aforementioned implementation of CIME infrastructure, CESM/WRF air–sea flux parameterization options and availability of full-functional CLM4 still make R-CESM unique and valuable. Two additional developments are underway (refer to the "Path forward" section for details), and the existing and upcoming capabilities of R-CESM will contribute significantly to high-resolution Earth system modeling studies and further applications.

R-CESM applications

This section illustrates three applications of R-CESM that focus on model climatology, extremes, and very small-scale air–sea interaction, respectively. Note that R-CESM results are compared with observations where appropriate, but not with other regional coupled model studies due to the inherent differences in the model settings and configurations such as domain sizes, initial and boundary conditions, run lengths, and physics and parameterization schemes.

Gulf of Mexico climate simulation. To illustrate R-CESM's ability to make long-term regional climate simulations without any flux adjustments or restoring, a 9-yr-long Gulf of Mexico (GOM) simulation for the 2010–18 period was performed without the use of any nudging in the interior of the model domain. For this experiment, the CESM air–sea flux scheme was applied. The GOM is an ideal testbed for such an evaluation because of the presence of dynamical ocean features like the Loop Current and Loop Current eddy (Oey et al. 2005) as well as strong air–sea interactions associated with hurricanes (Jaimes et al. 2016). This GOM R-CESM is configured with a 3-km ROMS and 9-km WRF (see section "Summary of R-CESM Experiments presented in this paper" in appendix A for details about model initial and boundary conditions).

Comparison of annual-mean R-CESM SST with that from the 1/20°-horizontal-resolution Group for High-Resolution Sea Surface Temperature (GHRSST; Donlon et al. 2007) product (Figs. 2a–c) shows that the R-CESM is able to simulate the mean distribution of SSTs in the Gulf of Mexico accurately with warmer (>27°C) SST in the Caribbean and Loop Current area and cooler waters (<25°C) along the coastal region. The difference between R-CESM and GHRSST is less than 0.25°C in most of the GOM, a significant improvement from global high-resolution models with biases of 0.5°–1°C (see Fig. 3 of Small et al. 2014). The seasonal cycle of SST along a representative longitude of 86°W (Figs. 2d–f) also shows that R-CESM simulates the extent of warm (June–November) and cold (December–May) seasons, with a minimum

Unauthenticated | Downloaded 08/28/24 03:34 AM UTC

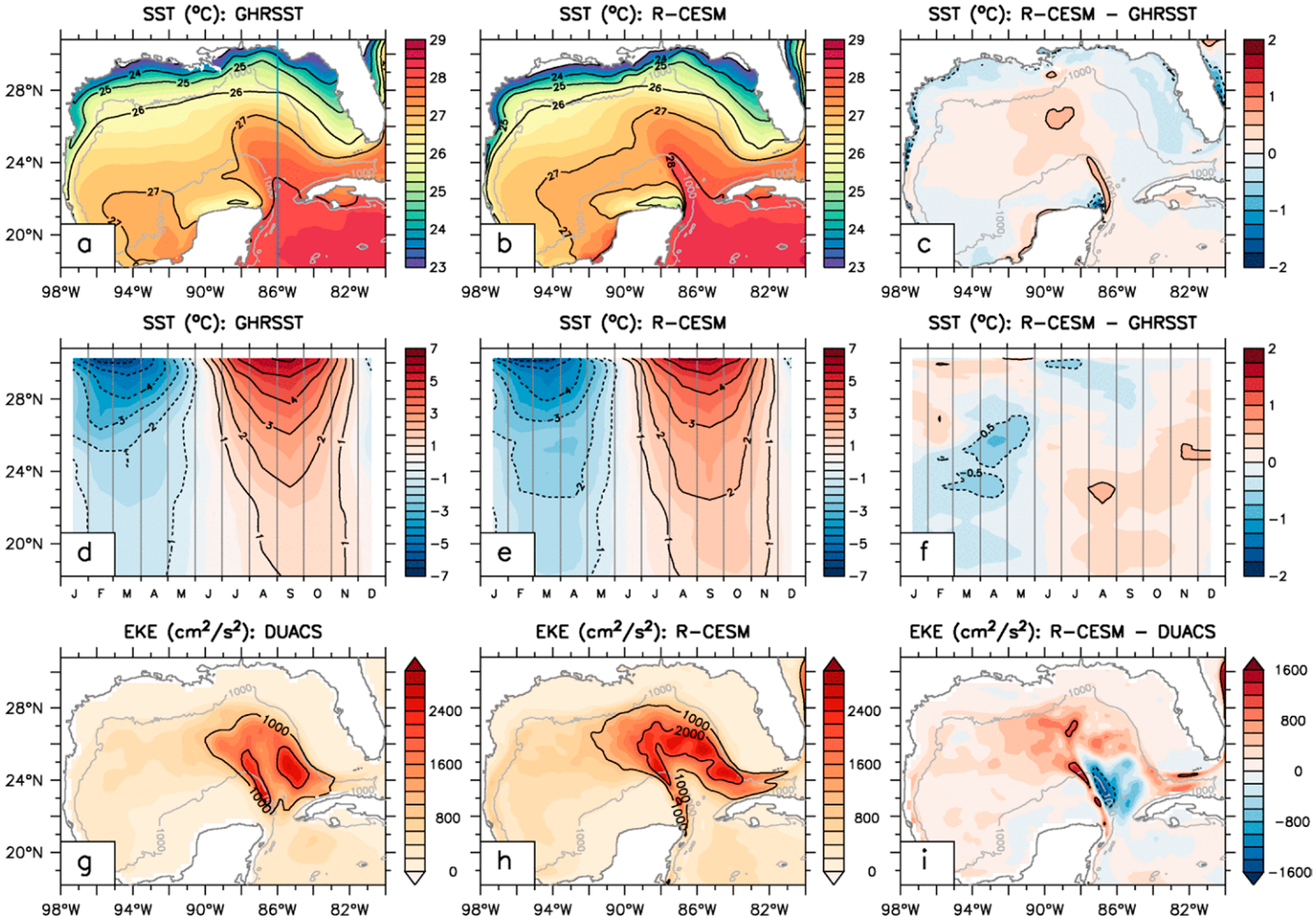

Fig. 2. Evaluation of 9-yr-long (2010–18) Gulf of Mexico R-CESM simulation using the CESM flux scheme. Annual mean SST (°C) from (a) GHRSST, (b) R-CESM, and (c) their difference. Seasonal cycle of SST (°C) along 86°W from (d) GHRSST, (e) R-CESM, and (f) their difference, and geostrophic EKE ($cm^2\ s^{-2}$) from (g) DUACS altimetry, (h) R-CESM, and (i) their difference. The blue line in (a) shows the 86°W longitude used for the SST seasonal cycle. SST seasonal cycle is shown using monthly climatology data, after removing the annual mean. The geostrophic EKE is computed from geostrophic currents estimated using sea surface height, and the R-CESM data have been spatially smoothed over a 24-km scale to match the resolution of the DUACS dataset.

SST in February–March and a maximum SST in August–September as in the observations (Muller-Karger et al. 2015). However, the seasonal amplitude of SST change is slightly higher in R-CESM (by ~0.25°C) to the south of about 26°N. To validate the simulated ocean dynamics in R-CESM, we compare the geostrophic eddy kinetic energy (EKE, $cm^2\ s^{-2}$) from 1/4°-horizontal-resolution daily DUACS (Data Unification and Altimeter Combination System, http://www.duacs.cls.fr/) altimetry data with that from R-CESM in Figs. 2g–i. As in the DUACS data, R-CESM shows elevated EKE in the Loop Current region with similar magnitudes.

R-CESM's fidelity in simulating atmospheric variability is examined by comparing the simulated precipitation with observations in Fig. 3. Over the continental United States, observed precipitation is based on the 4-km NCEP Stage IV data (Du 2011), while the 0.25° TRMM 3B42 (Huffman et al. 2007) is used in the rest of domain. From the annual-mean perspective, R-CESM generally reproduces the observed spatial patterns, especially over Texas and Oklahoma, but noticeably overestimates precipitation in high-altitude areas like the Appalachian Mountains and Sierra Madre, and also over Florida. Nevertheless, the present R-CESM yields a significant improvement in precipitation simulation compared to the global

Unauthenticated | Downloaded 05/28/24 03:34 AM UTC

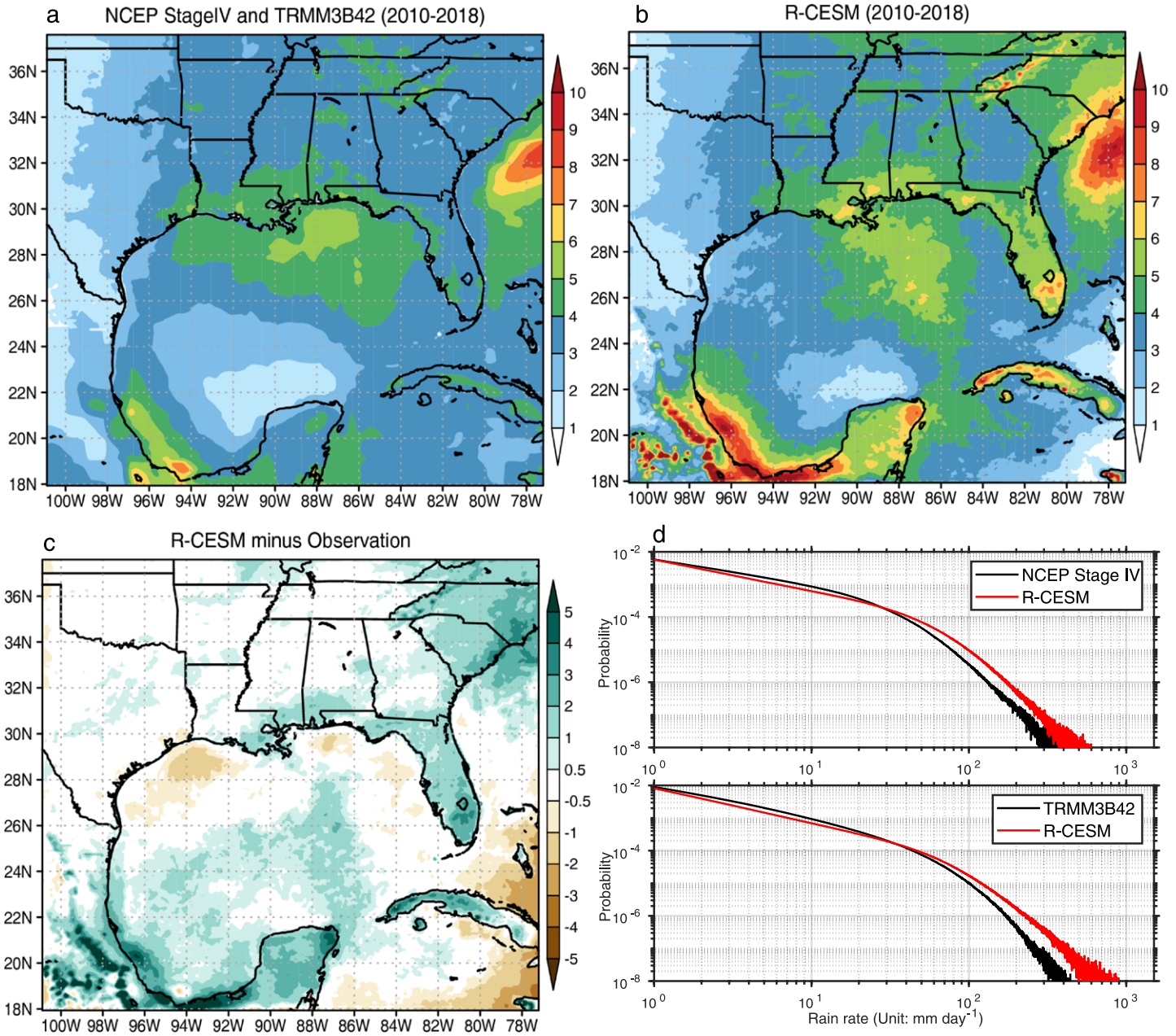

Fig. 3. Evaluation of 9-yr-long (2010–18) Gulf of Mexico R-CESM simulation using the CESM flux scheme. Annual mean precipitation (mm day^{-1}) from (a) the observation (NCEP Stage IV rain gauge in the continental United States and TRMM 3B42 for the rest area), (b) R-CESM and (c) difference of the two. (d) Probability distribution function of daily accumulated precipitation (mm day^{-1}) from the observations (black) and R-CESM (red).

high-resolution CESM1 simulation which shows dry biases over the southeast United States (e.g., see Fig. 13 in Bacmeister et al. 2014). Figure 3d further compares the probability distribution function (PDF) of daily accumulated precipitation from the observations and R-CESM simulation. The simulated frequency of weak-to-moderate precipitation (<40 mm day^{-1}) is remarkably consistent with the observations, but heavy precipitation (>40 mm day^{-1}) shows a positive bias, which contributes significantly to the simulated mean precipitation bias.

Comparisons of air–sea flux schemes in tropical cyclones simulation. As noted in the "WRF and CESM air–sea flux schemes options" section, one of the most important novelties of R-CESM is the ability to employ either the CESM or WRF air–sea flux schemes. To investigate whether the CESM air–sea flux scheme is suitable for simulating TCs compared to

Unauthenticated | Downloaded 05/28/24 03:34 AM UTC

the WRF scheme, we conducted two suites of TC hindcast simulations using R-CESM, one suite using the CESM scheme, the other the WRF scheme. The configuration employed a convection-permitting 3-km horizontal resolution (no nesting domain configuration) in the atmosphere and a submesoscale-permitting 3-km horizontal resolution in the ocean. Each suite of experiments considered 12 observed TC cases (appendix A) in the Gulf of Mexico with a seven-member ensemble for each TC case. Except the surface flux schemes, all other settings were the same, and the cumulus parameterization was turned off. The initial and boundary conditions for WRF and ROMS were directly derived from ERA5 (Hersbach et al. 2020) and Copernicus Marine Service global ocean data (see appendix A) without any data assimilation, and ensemble members were generated using Stochastic Kinetic Energy Backscatter (SKEB) scheme (Shutts 2005).

Figures 4a–c show the composite axisymmetric vertical structures of simulated TCs at their lifetime peak intensity for CESM and WRF schemes along with their difference. It is notable that the maximum tangential wind speed $V_{\max}$ simulated with the CESM flux scheme is significantly weaker than that of the WRF scheme by about 20%. Meanwhile, the radius of the maximum tangential wind speed at each vertical level as denoted by the blue lines in the figures, which represents the eyewall slope, shows a wider inner core with the CESM flux scheme, and thus a relatively weaker TC intensity and secondary circulation. Further, the TC-induced SST cooling by the surface wind drag in the CESM scheme is somewhat weaker than that in the WRF scheme (Figs. 4e,f), but both are colder than in observations (Fig. 4d). These TC peak intensity differences may partially be explained with the wind-induced surface heat exchange (WISHE) theory of Emanuel (1986, 1995): $V_{\max}$ is proportional to the ratio of enthalpy exchange coefficient (C_k) to the drag coefficient (C_D), and this ratio is smaller in the CESM flux scheme than in the WRF flux scheme (Fig. 4g), consequently resulting in weaker TCs with the CESM scheme.

The simulated TC maximum 10-m wind speed and minimum sea level pressure relationship formed by aggregating all 12 cases and their seven-member ensembles is shown in Fig. 4h, along with the best tracks of all TCs in the GOM during 1979–2018. Impressively, the WRF scheme yields a very similar best-fit curve to that from the observation, while the CESM scheme shows a notable problem: for a given pressure, the simulated 10-m wind speeds are too weak.

The present results suggest that the large-scale climate-oriented current CESM flux scheme systematically underestimates TC intensity compared to the WRF flux scheme that is developed specifically for weather applications. It should be noted that these suites of R-CESM TC simulations are performed with the nonhydrostatic WRF dynamic core at 3-km horizontal resolution, whereas the current highest-resolution CESM simulation (~14-km atmosphere) still uses a hydrostatic dynamical core. Thus, the above result of the CESM and WRF schemes for a convection-permitting 3-km grid may not be quantitatively applicable to climate models at coarser resolutions. However, these results still support the notion that the simulated TC intensity is highly sensitive to surface flux parameterizations, raising the question of whether a better TC pressure–wind relationship can be obtained if the current CESM flux scheme is modified following the suggestion in the appendix of Large and Yeager (2009) to cap off the drag coefficient at high wind speeds [see also Green and Zhang (2013) for discussion of the impact of capping the drag coefficient via altering the roughness length representation].

Although the WRF flux scheme shows remarkable consistency with the observed TC wind-pressure relationship in this study, we are not aiming to state the WRF flux scheme is the optimum choice, as the actual forms of surface exchange coefficients are still highly uncertain under high-wind conditions. A more comprehensive analysis, including assessing the role of capping drag coefficient of CESM flux scheme at high wind speeds in TC intensity, and its broader implications to CESM model will be presented in a separate study.

Unauthenticated | Downloaded 05/28/24 03:34 AM UTC

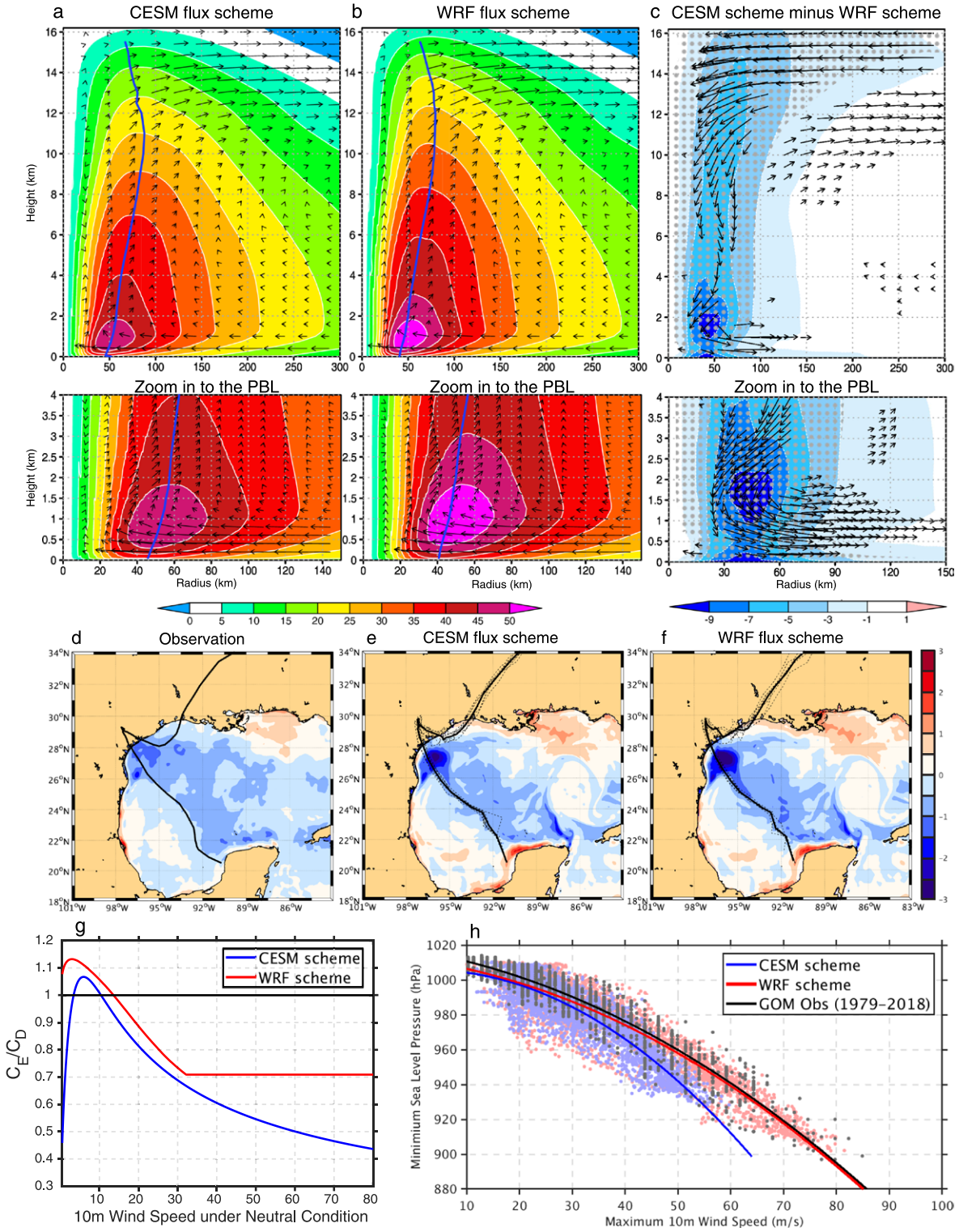

Fig. 4. Composite of azimuthally averaged distance–height cross sections of ensemble-mean tropical cyclone tangential wind speed (m s^{-1}; color shading) and secondary circulation (vectors; vertical velocity is scaled with a factor of 5 for clarity) at their lifetime peak intensity from (a) CESM, (b) WRF surface flux scheme, and (c) difference of the two. Gray dots highlight statistical confidence at the 95% level based on two-sided *t* test, and vector anomalies are plotted only where the confidence level is above 95%. The blue curve denotes the radius of maximum tangential wind speed at each vertical level. Hurricane Harvey (2017) induced SST anomaly (°C) from (d) observations, (e) CESM, and (f) WRF surface flux scheme. SST anomalies are calculated by using GHRSST or modeled seven-member ensemble mean on 26 Aug 2017 minus the 1–20 Aug 2017 mean. The observed and simulated ensemble-mean Harvey tracks are overlaid with solid black lines. Dashed lines indicate the individual ensemble member. (g) Neutral stability exchange coefficient ratios C_E/C_D from CESM (blue) Fig. 4. and WRF (red) flux scheme as the function of 10-m wind speed. (h) Scatterplot of TC maximum 10-m wind speed and minimum sea level pressure. Blue and red dots denote the 3-hourly R-CESM outputs from CESM and WRF flux scheme, respectively, while black dots indicate the 6-hourly observation from GOM. The least squares quadratic best-fit regression lines are also overlaid.

Unauthenticated | Downloaded 08/28/24 03:34 AM UTC

Air–sea coupling in a submesoscale-permitting simulation. Oceanic submesoscales have lateral scales of $O(1–10)$ km and a vertical scale proportional to the mixed layer depth (e.g., Capet et al. 2008; Fox-Kemper et al. 2008; Thomas et al. 2008). They are generated by several mechanisms fueled by available potential energy in the surface boundary layer (McWilliams 2016). A rich literature exists on air–sea interaction at $O(100)$-km oceanic mesoscale processes (e.g., Small et al. 2008; Chelton and Xie 2010). Similar studies at $O(1–10)$-km scales, however, are daunting due to the computational cost incurred in fully coupled ocean–atmosphere simulations at these resolutions (e.g., Byrne et al. 2015; Renault et al. 2018). We present here results from a downscaled coupled simulation of the Kuroshio region with boundary conditions from an existing 9-km North Pacific coupled simulation (Ma et al. 2016). Our simulation has a nominal resolution of 3 km for both the atmosphere and ocean, and thus permits oceanic submesoscales. We ran the R-CESM model for the duration 15 October 2003 to 29 March 2004. For statistics, we only use fields collected after the first two weeks.

Figure 5a shows the time-averaged wind work after applying a two-dimensional horizontal box filter to the wind stress and surface horizontal velocities at every model time step to retain only scales greater than 102 km. In R-CESM, the wind stress formulation within CIME takes into account the ocean surface currents. The wind work (Fig. 5a) is mostly positive due to the

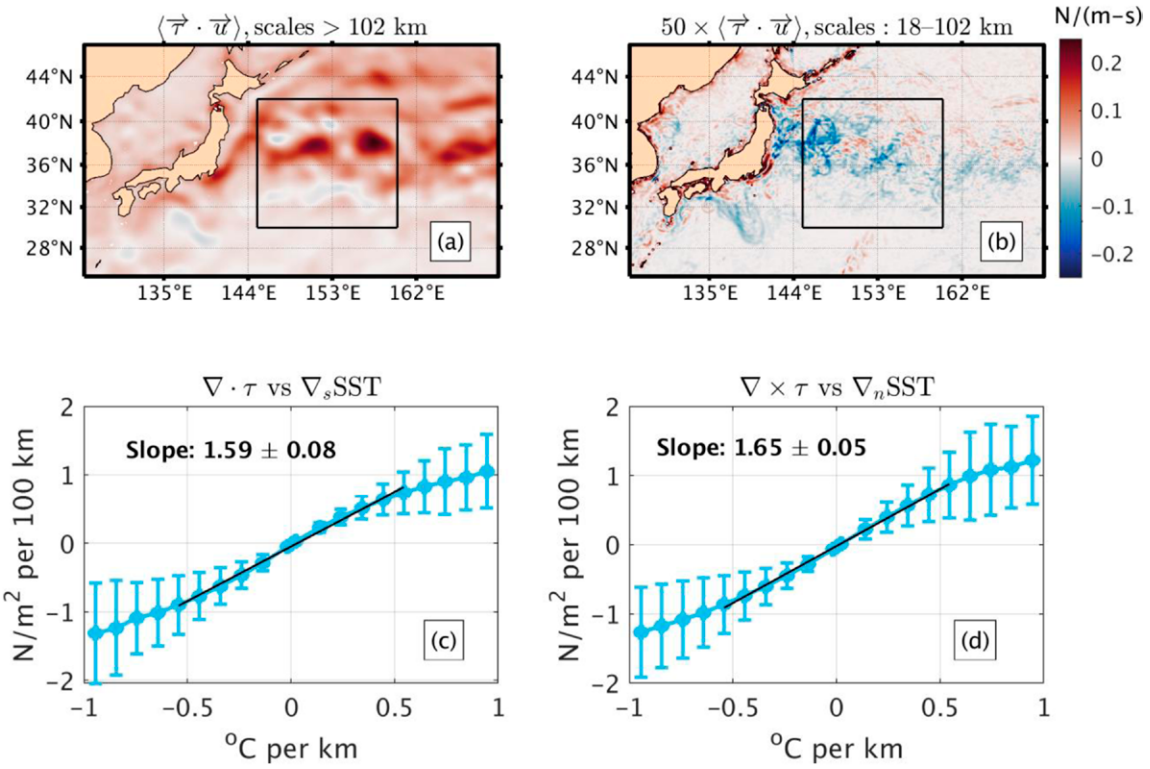

Fig. 5. (a) Time-averaged wind work at scales larger than 102 km. (b) As in (a), but for scales of 18–102 km (note the multiplying factor). The wind work in (a) and (b) are averages over the period 29 Oct 2003–29 Mar 2004. (c) Binned averages of wind divergence vs the downwind gradient of SST, here approximated using the model temperature at the shallowest level. The *s* subscript denotes the downwind direction. (d) As in (c), but for the wind curl and the crosswind gradient of SST, where the *n* subscript denote the crosswind direction. The vertical bars show the standard deviation within each bin and the black lines represent linear best fits for the binned averages, valid for SST gradients spanning the range ±0.5°C km^{-1}. The slopes are statistically significant at the 95% confidence level and the 95% confidence intervals are indicated along with the slope. The binned averages have been obtained from fields collected within the black box identified in (a) and (b) and over the same duration as that used for the time averaging.

Unauthenticated | Downloaded 05/28/24 03:34 AM UTC

atmosphere energizing the ocean at large scales. This sharply contrasts the wind work for scales between 18 and 102 km (Fig. 5b). The magnitude of wind work at these scales is considerably smaller compared to that at larger scales. Away from the coast, the strongest values are negative in sign and occur in eddy-rich areas in the vicinity of the Kuroshio Extension. A corresponding plot for scales 3–18-km (not shown) bears similar features, namely, decreasing magnitudes compared to larger scales but negative values dominating positive values. The negative values denote an energy sink, a transfer of kinetic energy from the ocean to the atmosphere. These results therefore show a reversal in the direction of coupling at scales finer than 100 km.

Figures 5c and 5d show binned averages of (i) the wind stress divergence [in N m^{-2} $(100\ km)^{-1}$] versus the downwind SST gradient (in °C km^{-1}) and (ii) the wind stress curl versus the crosswind SST gradient. We populate the bins using instantaneous values of the gradients in the wind stress and SST within the region identified by the black box (Figs. 5a,b) at every model time step, before computing the average within each bin. The nearly linear relationship among the binned averages of each of these pairs of variables at the mesoscales has received considerable attention in the literature (e.g., Chelton et al. 2001; Seo et al. 2007; Small et al. 2008; Song et al. 2009; Bryan et al. 2010; Putrasahan et al. 2013; Schneider and Qiu 2015). These studies show a larger slope for the response of the wind stress divergence to the downwind SST gradient compared to that describing the response of the wind stress curl to the crosswind SST gradient. The oceanic and atmospheric grid resolutions in the studies cited above are coarser than that used in our simulations (i.e., 3 km). Our results reproduce the linear relationship (Figs. 5c,d) with a couple of noteworthy differences. The downwind and crosswind SST gradients induce comparable responses in the wind stress divergence and curl, respectively, as measured by the regression slope. Second, the magnitude of the slope for either regression is considerably larger than those reported with coarser oceanic/atmospheric resolutions, e.g., 1.59 (Fig. 5c) versus 0.75 (see Table 2 in Bryan et al. 2010) and 1.65 (Fig. 5d) versus 0.53 (Bryan et al. 2010). These differences show stronger air–sea coupling in the presence of an oceanic submesoscale field. For reference, an SST gradient of 0.5°C km^{-1} corresponds to a lateral buoyancy gradient $O(10^{-6})$ s^{-2}, typical of strong density fronts observed in the Kuroshio (D'Asaro et al. 2011). Hence, the regression presented here spans a range of SST gradients of relevance to that region. The results in this section convey the utility of R-CESM as an effective platform to study air–sea interactions at submesoscales within a fully coupled framework.

Path forward

Two active areas are under development to advance the capabilities of the R-CESM system.

E-CESM. In certain situations, it is desirable to have a two-way interaction between the global and regional model by running them simultaneously. This infrastructure has been tested within the R-CESM framework by enabling two different models for the same component, i.e., the Parallel Ocean Program version 2 (POP2, see appendix A) and ROMS for the ocean component, in the Embedded CESM (E-CESM, Fig. 6a). A key aspect of E-CESM is that SSTs from the two ocean models are merged before passing them to CIME to compute surface fluxes at every air–sea coupling time step (Fig. 6a). This merging is done on a multiscale coupling grid: a nonuniform grid with ROMS grid points where ROMS exists and POP grid points outside of it (Fig. 6b). Meanwhile the two ocean models communicate below the surface in two steps: ROMS receives lateral boundary conditions from POP2, and then the POP2 three-dimensional temperature and salinity are restored toward that of ROMS in the region of the ROMS domain. E-CESM will be provided within the R-CESM framework via github, but is essentially a separate module allowing global simulations with some regional detail.

Unauthenticated | Downloaded 08/28/24 03:34 AM UTC

This embedding technique has only been tested on the ocean component, but the method is generic and, theoretically, can be adapted for other components in the future. Prototype simulations have so far incorporated a ROMS domain for the GOM embedded in the standard

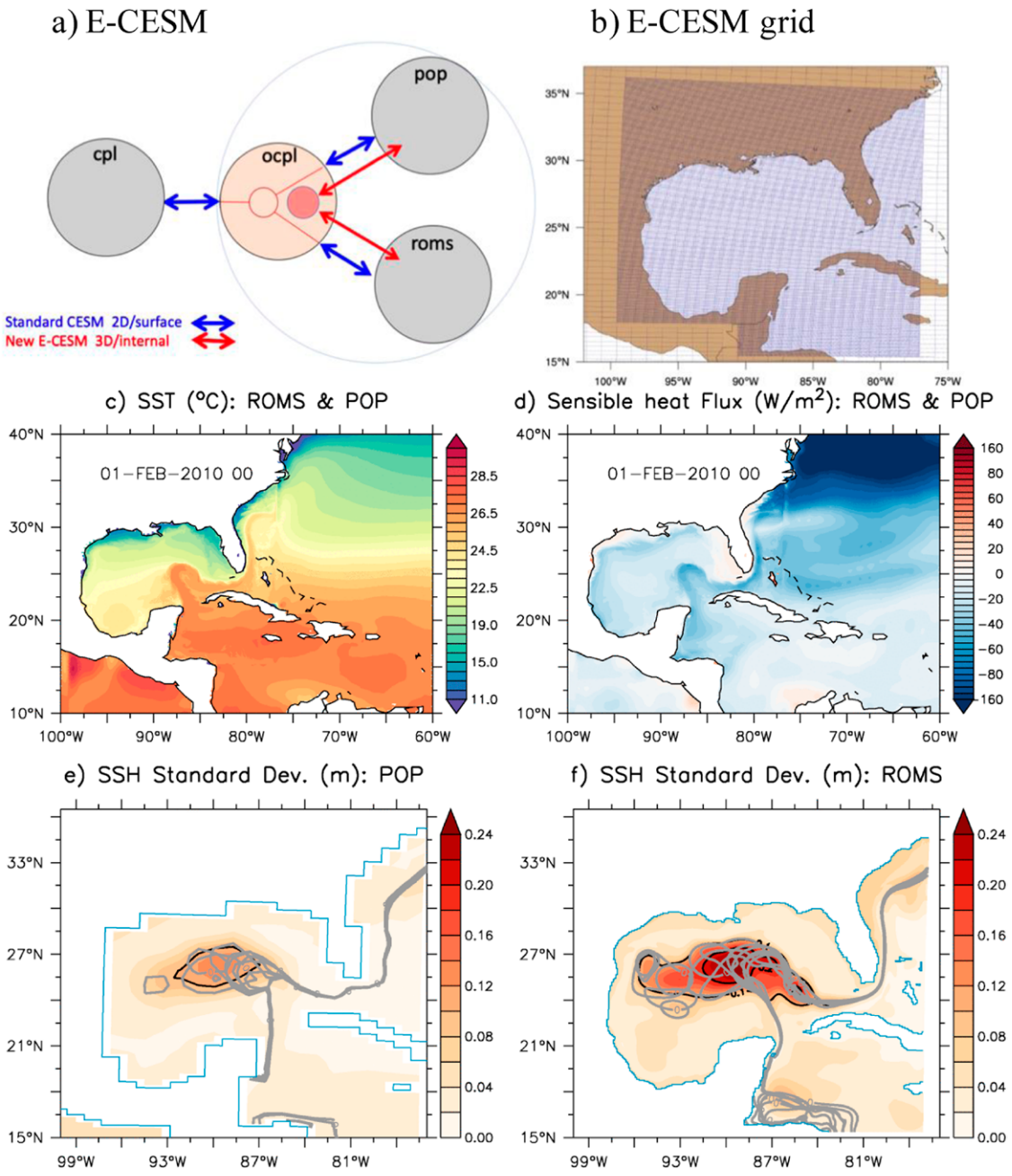

Fig. 6. E-CESM. (a) Schematic showing the coupling between ROMS, POP, a specially designed ocean coupler (ocpl), and the main CESM coupler (cpl, i.e., the CIME hub of Fig. 1). Blue arrows denote exchange of standard coupler variables such as SST, ocean surface current, and surface flux, while red arrows denote communication of 3D oceanic variables such as temperature, salinity, and zonal and meridional currents, as well as some 2D variables (sea surface height, barotropic currents). Merging of SST is done in the ocpl. The enclosed region within the thin gray circle replaces the single POP component of standard CESM. (b) Example design of a multiscale coupling grid, focusing on the Gulf of Mexico. (c) An example SST field on the multiscale grid, showing fine detail of the Loop Current and a smoother field outside of the ROMS domain and (d) the corresponding sensible heat flux on the multiscale grid, showing enhanced surface flux over the warm SST of the Loop Current, in addition to a strong cold-air outbreak off the U.S. East Coast giving rise to large fluxes (negative fluxes cool the ocean). Note that the color bar is nonlinear to highlight these two processes. (e) Standard deviation of SSH variability (colors, m) and individual seasonal-mean 0-m SSH contours (gray) from POP. (f) As in (e), but for ROMS.

Unauthenticated | Downloaded 05/28/24 03:34 AM UTC

nominal 1°-horizontal-resolution POP2 (Fig. 6b), for a 2-yr run. These simulations show mesoscale details in ROMS, such as the Loop Current, which are poorly resolved in POP2, and which are imprinted on the SST and thus surface heat flux field on the multiscale grid, allowing for suitable air–sea feedbacks (Figs. 6c,d). The standard deviation of sea surface height (SSH) in POP2 and ROMS components of the E-CESM simulation reaches maxima of about 14 and 24 cm, respectively (Figs. 6e,f, shading), the latter being comparable to observations (Small et al. 2014). Further, both components show Loop Current variability and eddy shedding (overlain gray contours): the 9-km ROMS can resolve these features, while for POP2 these features are due to the restoring of temperature and salinity to the regional model, as the standard POP2 in CESM lacks such variability (Small et al. 2014). It can be noted that there is some discontinuity at the eastern boundary (~76°W) in Figs. 6c,d as the fields transition from ROMS to POP2, which can be attributed to the large grid change (from 1° to 9 km) in the dynamic Gulf Stream region. A more ambitious but necessarily more computationally expensive future effort is to embed 3-km ROMS in the global high-resolution POP, at a nominal 0.1° horizontal resolution: the smaller transition in grid size should allow for smoother boundaries and let mesoscale ocean features enter the ROMS domain.

Another exciting new prospect would be to combine the above ocean setup with one of the CESM atmosphere components with mesh refinement, such as CAM-SE (e.g., as used by Zarzycki and Jablonowski 2014), so that both the ocean and atmosphere are similarly refined over a particular region.

"Online" ensemble coupled data assimilation. Although both ROMS and WRF have built-in data assimilation capability, assimilation can only be performed in an uncoupled mode (i.e., separately in each component) and is not compatible with our coupling framework. Thus, another ongoing R-CESM effort is to develop an ensemble-based coupled data assimilation (ECDA) capability for obtaining accurate and coherent initial conditions for regional prediction applications. The "online" ECDA procedure developed by Zhang et al. (2005, 2007), which embeds an ensemble Kalman filter algorithm into a forecast model as a set of subroutines, is one of the most promising techniques for ECDA in terms of computational efficiency.

We have implemented the "online" ECDA into R-CESM with preliminary evaluation using ocean surface observations with the same model configuration discussed in the "Gulf of Mexico climate simulation" section. Besides the free GOM simulation, we also assimilated the observed SSH using "online" ECDA. Figure 7 shows the SSH snapshots on 11 June 2010 in observations and various model simulations. Observations show a Loop Current eddy-shedding event (Fig. 7a), while the Loop Current eddy in the R-CESM free run (without data assimilation) shows some unrealistic features with eddy-related SSH extending too far north in the GOM, and too-low SSH in the coastal regions (Fig. 7b). Compared to the free run, the data assimilation run clearly shows an improved representation of the main Loop Current eddy shedding and coastal SSH that is in good agreement with observations (Fig. 7c). To evaluate this improvement in practical forecast applications, we conducted another free run initialized using the restart file on 30 May 2010 from the data assimilation run, which provides better initial conditions than the free run, and produced a successful prediction of Loop Current eddy-shedding event at a lead time of 12 days (Fig. 7d).

A suite of code developments and more evaluation ECDA experiments are on the way, and we plan to provide the "online" ECDA capability to the community in our next model release.

Summary

R-CESM is a novel system that allows the use of regional models of high resolution within the CESM framework. The advantages that come with this new system include, but are not

Unauthenticated | Downloaded 08/28/24 03:34 AM UTC

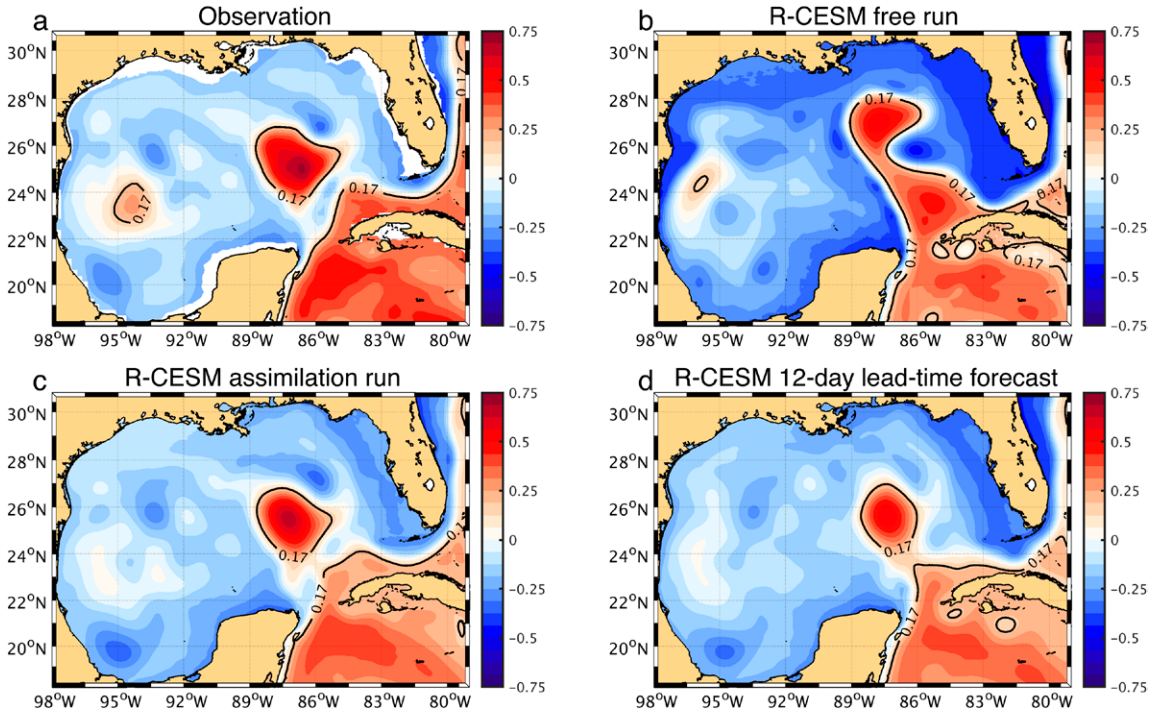

Fig. 7. The snapshots of sea surface height (SSH; m) on 11 Jun 2010 in the (a) observations, (b) R-CESM free simulation without data assimilation, and (c) R-CESM simulation with data assimilation. (d) R-CESM forecasted SSH on 11 Jun 2010 using model initial conditions from the R-CESM data assimilation run restart files on 30 May 2010 (12-day lead-time forecast). The Loop Current eddy-shedding event is defined based on the 0.17-m SSH closed contour.

limited to (i) being open source, and having a potentially broad user base through its connection with CESM; (ii) use of the CIME infrastructure to connect WRF, ROMS, CLM4, and other CESM2 component models, and has extensive configuration flexibility; and (iii) embedding of regional models within global CESM2 configurations.

A few illustrative examples of the applications of R-CESM have been given. A 9-yr-long control integration revealed high fidelity in simulating GOM regional climate, considering key variables such as SST, precipitation, and ocean EKE. An ensemble of TC hindcast simulations allowed for assessment of the ability of R-CESM in capturing TC statistics at a 3-km resolution, with nonhydrostatic atmospheric physics, explicit convection, and different air–sea flux schemes. Submesoscale ocean processes were permitted in a 3-km-resolution coupled simulation of the Kuroshio region.

One of the major results of the study was that the WRF air–sea flux scheme, with the drag coefficients capped at high wind speeds, gave stronger TC intensity and more realistic surface pressure–wind relationships than the CESM air–sea flux scheme. Although we have only tested this finding in the nonhydrostatic regime (<10-km resolution), the result should also be of interest to global climate modelers using the CESM air–sea flux scheme at TC-permitting resolutions (~25 km).

In new developments, we have shown that the high-resolution ROMS could be embedded in a global ocean model POP2, in a configuration that allows simple two-way ocean feedbacks as well as a new multiscale coupling grid to communicate with the atmosphere. Further work is also ongoing with the "online" ensemble coupled data assimilation capability in the R-CESM system, and we seek to provide more comprehensive regional weather and climate forecast and reanalysis products in the future.

Further development of the R-CESM will include taking advantage of the CESM2 framework to include other component models (such as sea ice, river runoff) and enhanced capabilities to couple regional-in-global models (e.g., ROMS in POP2 coupled to CAM6). The paper has

Unauthenticated | Downloaded 05/28/24 03:34 AM UTC

illustrated just a few examples of R-CESM applications—clearly it would be ideal to test it for many different regions and cases, and it is hoped that the potential user-base community (including the CESM community) can contribute to this. By broadening the usage and with a regular update cycle the R-CESM should become a valuable tool to aid both global and regional ESM development.

Acknowledgments. This is a collaborative project between the Ocean University of China (OUC), Texas A&M University (TAMU), and the National Center for Atmospheric Research (NCAR) and completed through the International Laboratory for High-Resolution Earth System Prediction (iHESP)—a collaboration between the Qingdao National Laboratory for Marine Science and Technology (QNLM), TAMU, and NCAR. The early development of R-CESM was supported by the National Science Foundation (NSF) Grants AGS-1067937 and AGS-1347808, Department of Energy Grant DE-SC0006824, as well as National Oceanic and Atmospheric Administration Grant NA11OAR4310154 to TAMU. NCAR is a major facility sponsored by the NSF under Cooperative Agreement 1852977. The authors would like to acknowledge the Texas A&M High Performance Research Computing (HPRC) and the Texas Advanced Computing Center (TACC) for providing advanced computing resources that have contributed to the research results reported within this paper. Our open-source framework is publicly available at https://github.com/ihesp/rcesm1. We especially acknowledge the fundamental contributions from Raffaele Montuoro to the early development of R-CESM, which was critical to the success of the R-CESM project.

Data availability statement. Information to obtain the datasets required to set up and run the R-CESM Gulf of Mexico test cases are provided with the R-CESM source code, which is available at https://github.com/ihesp/rcesm1. The model results presented in this paper can be requested by contacting the corresponding authors.

Appendix A: Model configurations

ROMS. ROMS (Haidvogel et al. 2008; Shchepetkin and McWilliams 2005) is a primitive equation, hydrostatic, free-surface, split-explicit ocean model with horizontal curvilinear coordinates and terrain-following "z–sigma" vertical coordinates (Lemarié et al. 2012; Shchepetkin and McWilliams 2009). The ROMS component of R-CESM uses identical settings in all configurations: harmonic horizontal mixing of momentum and tracers, the K-profile parameterization (KPP) scheme (Large et al. 1994) for vertical mixing, the fourth-order Akima horizontal and vertical tracer advection (Shchepetkin and McWilliams 2005), and 50 layers in the vertical. ROMS receives surface fluxes from CIME. Open boundary conditions are configured with radiation and nudging schemes for the three-dimensional velocity and tracers, Chapman (1985) scheme for the free surface, and Flather (1976) scheme for the two-dimensional velocities.

The ROMS domain in R-CESM is designed to be slightly smaller than that of WRF (Figs. 1c,d) so that the WRF boundary artifacts (due to a dynamic inconsistency between WRF's interior solution and prescribed lateral boundary conditions) do not affect the actively coupled ROMS region. To provide SST for the gap region between ROMS and WRF domains, a new X-ROMS (extended-ROMS) horizontal grid, which covers the WRF domain with matching grid points with ROMS grid over the overlapping region, has been used. The X-ROMS blends SST from ROMS with that provided from data [on X-ROMS grid, from the dataset used for ROMS initial and boundary conditions] before passing it to the coupler.

WRF. The Advanced Research version of the WRF Model (Skamarock et al. 2008) is a fully compressible, Eulerian, nonhydrostatic atmospheric model with a terrain-following vertical coordinate. In this initial release of R-CESM, the incorporated WRF version is 3.5.1. Besides

Unauthenticated | Downloaded 05/28/24 03:34 AM UTC

the inherited flexibility from original WRF (only three surface-layer schemes are available in the first release), WRF in the R-CESM configuration is also capable of receiving air–sea fluxes from CIME and bypass the WRF built-in surface-layer subroutines, which is one of the unique features in our open-source system. In this work, all the simulations are conducted with the Yonsei University (YSU) planetary boundary layer scheme (Hong et al. 2006), Purdue–Lin microphysics scheme (Lin et al. 1983), Rapid Radiative Transfer Model for GCMs (RRTMG) shortwave and longwave radiation schemes (Iacono et al. 2008). No cumulus parameterization is utilized in any set of experiments.

CLM4. CLM4 is the standard land component in the R-CESM system. There are several key differences between native CLM4 and WRF built-in CLM4 package. As of WRF3.5.1, lake and urban canopy models, including CLM4 urban parameterization (CLMU; Oleson et al. 2010b), are not available in WRF built-in CLM4, whereas they are actively working in R-CESM. This is of critical importance to assess the regional climate, as high population density makes urban climate significantly different from other land surface area and may have discernible impacts on the regional climate (Zhao et al. 2021). Second, the number of vertical soil levels in WRF CLM4 is 10 but it is 15 in R-CESM CLM4. Third, WRF CLM4 is "cold" started by direct interpolation of soil data from atmospheric reanalysis products (typically 4 vertical layers) using the WRF preprocessing system, while R-CESM CLM4 is first integrated for 10 years using the surface atmospheric forcing from reanalysis (CESM data atmosphere) products as spinup to "warm" start.

POP2 (used in E-CESM). POP2 is on a nominal 1° grid [1.125° in the zonal direction and meridionally between 0.27° at the equator and 0.54° at higher latitudes]. It has 60 vertical levels, with a 10-m grid spacing in the upper 100 m. The main parameterizations are of vertical mixing (KPP; Large et al. 1994), mesoscale eddies (Gent and McWilliams 1990), submesoscale eddies (Fox-Kemper et al. 2008), and dense overflows (Danabasoglu et al. 2012).

Summary of R-CESM Experiments presented in this paper. For sections "Gulf of Mexico climate simulation" and "Comparisons of air–sea flux schemes in tropical cyclones

Table A1. Details of R-CESM model experiments presented in this paper.

Experiment name	Section in the paper	Model domain	Horizontal resolution (km)		Surface flux scheme	Simulation period
			ROMS	WRF		
Long-time climate control	"Gulf of Mexico climate simulation"	Gulf of Mexico	3	9	CESM	0000 UTC 1 Jan 2010–2100 UTC 31 Dec 2018
Flux comparison using tropical cyclones	"Comparisons of air–sea flux schemes in tropical cyclones simulation"	Gulf of Mexico	3	3	CESM	At least 4 days, varies with case
Flux comparison using tropical cyclones	"Comparisons of air–sea flux schemes in tropical cyclones simulation"	Gulf of Mexico	3	3	WRF	At least 4 days, varies with case
Submesoscale ocean processes	"Air–sea coupling in a submesoscale-permitting simulation"	Kuroshio Extension	3	3	WRF	0000 UTC 1 Oct 2010–1800 UTC 31 Mar 2004

Unauthenticated | Downloaded 09/28/24 03:34 AM UTC

simulation," daily data from the Copernicus reanalysis (product 001_025 for 2010–15 and product 001_030 for 2016–18) from E.U. Copernicus Marine Service Information are used for ROMS initial and boundary conditions. Six-hourly CFSR (Saha et al. 2010; March 2010/11), CFSv2 (Saha et al. 2014; April 2011–18), and ERA5 are used to obtain WRF initial and boundary conditions in sections "Gulf of Mexico climate simulation" and "Comparisons of air–sea flux schemes in tropical cyclones simulation," respectively. The sampled 12 intense TCs in the "Comparisons of air–sea flux schemes in tropical cyclones simulation" section include major hurricanes (category 3 and above) Michael (2018), Harvey (2017), Isaac (2012), Rita (2005), Katrina (2005), Lili (2002), Bret (1999), and Opal (1995) and relatively weak hurricanes (category 1 and 2) Hermine (2016), Dolly (2008), Claudette (2003), and Earl (1998). For section "Air–sea coupling in a submesoscale-permitting simulation," existing R-CESM results for the North Pacific at 9-km resolution (Ma et al. 2016) are used for ROMS and WRF initial and boundary conditions. See Table A1 for more information.

Appendix B: WRF and CESM air–sea flux schemes

WRF hosts seven surface layer schemes based on various observational and theoretical studies as of the version 3.5.1 used in R-CESM. Out of these seven, three are available with the first public release of R-CESM, namely, the MM5 Monin–Obukhov scheme (Zhang and Anthes 1982), revised MM5 Monin–Obukhov scheme (Jiménez et al. 2012), and Pleim–Xiu surface layer scheme (Pleim and Xiu 1995). For simplicity, in this paper, we only discuss the MM5 Monin–Obukhov scheme (Zhang and Anthes 1982) with modified Charnock's relation based on Donelan et al. (2004). Note that CESM2 has single air–sea flux parameterization scheme (referred to as the CESM air–sea flux scheme),

At a fundamental level the CESM and WRF schemes are both based on the Monin–Obukhov similarity theory (Monin and Obukhov 1954; reviewed, e.g., in Large 2006), where the vertical wind shear and vertical gradients of heat and moisture follow universal functions based on a stability parameter. Differences between the CESM and WRF schemes lie in how certain key features are formulated, summarized here in brief. The CESM scheme over ocean is based on semiempirical forms of the neutral exchange coefficients for momentum (drag coefficient) and sensible and latent heat (Large and Pond 1981, 1982; Large and Yeager 2004, 2009). Here we note that "neutral" refers to the value that would be observed under neutral air–sea stratification of buoyancy. In contrast to CESM, the WRF scheme does not explicitly prescribe the neutral exchange coefficients. Instead, the roughness lengths of momentum, and also those of heat and moisture are defined and computed. These denote the height at which a variable (wind or heat or moisture) reaches its surface value, in the well-known logarithmic form of the vertical profiles. The roughness length z_0 and the neutral drag coefficient at 10 m (C_{Dn}) are directly related by $z_0 = 10\exp\left(-\kappa/\sqrt{C_{Dn}}\right)$, where κ is the von Kármán constant. Thus, either prescribing the drag coefficient (basis for CESM scheme) or computing roughness lengths (basis for WRF scheme) can be used for computing fluxes and profiles, but with quantitative differences depending on how they are defined. In addition to the differences in the formulation of neutral exchange coefficients, the atmospheric stability correction function in the CESM scheme considers only two regimes (stable and unstable), while the WRF scheme yields four regimes (stable, mechanical driven turbulence, forced convection, and free convection), and thus is more comprehensive (see Table B1).

To use the CESM surface flux scheme from CIME with WRF, the flux coupler in CIME had to be adapted to compute and output several additional variables needed by the WRF boundary layer scheme. Those variables are listed in Table B1.

Unauthenticated | Downloaded 08/28/24 03:34 AM UTC

Table B1. The additional variables needed by the WRF to use CESM surface flux scheme.

Variable/Field	Description (What does variable measure/represent and for what purpose is it needed in WRF?)	Equation references	Variable name in WRF	Variable name in CESM
Bulk Richardson number	Measure of air–sea stability; used to define REGIMES of stability	e.g., over ocean: Zhang and Anthes [1982, Eq. (17)]; over land: Eq. (5.47) of Oleson et al. (2010a)	BR	BR (new)
Roughness length	A measure of roughness, strictly where the winds reach their surface value; used in log form of vertical profiles etc.; often termed z_0	Derived from neutral drag coefficient	ZNT	ZNT (new)
Stability parameter	Height divided by the Monin–Obukhov length, a key parameter in Monin–Obukhov similarity theory and flux scheme; a measure of stability; often termed ζ	e.g., Large and Yeager [2004, Eq. (8a)] and Large [2006, Eqs. (15) and (16)]	ZOL	hol
10-m actual wind velocity	10-m winds under actual stability (not neutral equivalent)	See footnote[a]	U10, V10	U10, V10 (new)
Friction velocity	Required in WRF PBL scheme	Large and Yeager [2004, Eq. (7a)]	UST	ustar
Integrated similarity functions	Integrated versions of the similarity functions; often termed ψ; used to determine the profile	e.g., Large and Yeager [2004, Eq. (8c)–(8e)]	PSIM, PSIH	psim, psih
Similarity functions	Functions of the stability parameter; used to determine the vertical shear; often termed ϕ	See footnote[b]	FM, FH	FM, FH (new)
Stability regime	Four regimes based on bulk Richardson number; describes the type of stability	e.g., Zhang and Anthes (1982, sections 2c,d)	REGIME	REGIME (new)

[a] Derived from $W_{10} = W_{z_{\text{bot}}} \times \left\{1 + \left(\sqrt{C_D}/\kappa\right)\left[\ln\left(10/z_{\text{bot}}\right) + \phi_m\left(z_{\text{bot}}\right) - \phi_m\left(10\right)\right]\right\}$ where W_z, is wind speed at height z, z_{bot} is the level of the model state variables (lowest model level), and C_D is drag coefficient at that same level and stability. The wind direction at 10 m is assumed the same as at z_{bot}.

[b] Derived from the integrated similarity functions ψ, e.g., for momentum $m = \ln z_{\text{bot}}\ z_0 - m$, where z_0 is roughness length and z is height. For heat and moisture, it uses a similar form with roughness length for heat and moisture derived from Eqs. (9), (12), and (13) of Large and Yeager (2009).

Unauthenticated | Downloaded 05/28/24 03:34 AM UTC

References

Bacmeister, J. T., M. F. Wehner, R. B. Neale, A. Gettelman, C. Hannay, P. H. Lauritzen, J. M. Caron, and J. E. Truesdale, 2014: Exploratory high-resolution climate simulations using the Community Atmosphere Model (CAM). *J. Climate*, **27**, 3073–3099, https://doi.org/10.1175/JCLI-D-13-00387.1.

Bell, M. M., M. T. Montgomery, and K. A. Emanuel, 2012: Air–sea enthalpy and momentum exchange at major hurricane wind speeds observed during CBLAST. *J. Atmos. Sci.*, **69**, 3197–3222, https://doi.org/10.1175/JAS-D-11-0276.1.

Bryan, F. O., B. G. Kauffman, W. G. Large, and P. R. Gent, 1996: The NCAR CSM Flux coupler. NCAR Tech. Note NCAR/TN-424+STR, 53 pp., https://doi.org/10.5065/D6QV3JG3.

——, R. Tomas, J. Dennis, D. Chelton, N. Loeb, and J. McClean, 2010: Frontal scale air–sea interaction in high-resolution coupled climate models. *J. Climate*, **23**, 6277–6291, https://doi.org/10.1175/2010JCLI3665.1.

Byrne, D., L. Papritz, I. Frenger, M. Munnich, and N. Gruber, 2015: Atmospheric response to mesoscale sea surface temperature anomalies: Assessment of mechanisms and coupling strength in a high-resolution coupled model over the South Atlantic. *J. Atmos. Sci.*, **72**, 1872–1890, https://doi.org/10.1175/JAS-D-14-0195.1.

Capet, X., J. C. McWilliams, M. J. Molemaker, and A. F. Shchepetkin, 2008: Mesoscale to submesoscale transition in the California Current System. Part I: Flow structure, eddy flux and observational tests. *J. Phys. Oceanogr.*, **38**, 29–43, https://doi.org/10.1175/2007JPO3671.1.

Cassano, J. J., and Coauthors, 2017: Development of the Regional Arctic System Model (RASM): Near-surface atmospheric climate sensitivity. *J. Climate*, **30**, 5729–5753, https://doi.org/10.1175/JCLI-D-15-0775.1.

Chang, P., and Coauthors, 2020: An unprecedented set of high-resolution earth system simulations for understanding multiscale interactions in climate variability and change. *J. Adv. Model. Earth Syst.*, **12**, e2020MS002298, https://doi.org/10.1029/2020MS002298.

Chapman, D. C., 1985: Numerical treatment of cross-shelf open boundaries in a barotropic coastal ocean model. *J. Phys. Oceanogr.*, **15**, 1060–1075, https://doi.org/10.1175/1520-0485(1985)015<1060:NTOCSO>2.0.CO;2.

Chelton, D. B., and S.-P. Xie, 2010: Coupled ocean-atmosphere interaction at oceanic mesoscales. *Oceanography*, **23**, 52–69, https://doi.org/10.5670/oceanog.2010.05.

——, S. K. Esbensen, M. G. Schlax, N. Thum, and M. H. Freilich, 2001: Observations of coupling between surface wind stress and sea surface temperature in the eastern tropical Pacific. *J. Climate*, **14**, 1479–1498, https://doi.org/10.1175/1520-0442(2001)014<1479:OOCBSW>2.0.CO;2.

Chen, S., T. J. Campbell, H. Jin, S. Gaberšek, R. M. Hodur, and P. J. Martin, 2010: Effect of two-way air–sea coupling in high and low wind speed regimes. *Mon. Wea. Rev.*, **138**, 3579–3602, https://doi.org/10.1175/2009MWR3119.1.

Curcic, M., and B. K. Haus, 2020: Revised estimates of ocean surface drag in strong winds. *Geophys. Res. Lett.*, **47**, e2020GL087647, https://doi.org/10.1029/2020GL087647.

Danabasoglu, G., S. C. Bates, B. P. Briegleb, S. R. Jayne, M. Jochum, W. G. Large, S. Peacock, and S. G. Yeager, 2012: The CCSM4 ocean component. *J. Climate*, **25**, 1361–1389, https://doi.org/10.1175/JCLI-D-11-00091.1.

——, and Coauthors, 2020: The Community Earth System Model Version 2 (CESM2). *J. Adv. Model Earth Syst.*, **12**, e2019MS00191, https://doi.org/10.1029/2019MS001916.

D'Asaro, E., C. Lee, L. Rainville, R. Harcourt, and L. Thomas, 2011: Enhanced turbulence and energy dissipation at ocean fronts. *Science*, **332**, 318–322, https://doi.org/10.1126/science.1201515.

Delworth, T. L., and Coauthors, 2012: Simulated climate change in the GFDL CM2.5 high-resolution coupled climate model. *J. Climate*, **25**, 2755–2781, https://doi.org/10.1175/JCLI-D-11-00316.1.

Donelan, M. A., B. K. Haus, N. Reul, W. J. Plant, M. Stiassnie, H. C. Graber, O. B. Brown, and E. S. Saltzman, 2004: On the limiting aerodynamic roughness of the ocean in very strong winds. *Geophys. Res. Lett.*, **31**, L18306, https://doi.org/10.1029/2004GL019460.

Donlon, C., and Coauthors, 2007: The global ocean data assimilation experiment high-resolution sea surface temperature pilot project. *Bull. Amer. Meteor. Soc.*, **88**, 1197–1214, https://doi.org/10.1175/BAMS-88-8-1197.

Du, J., 2011: GCIP/EOP surface: Precipitation NCEP/EMC 4KM Gridded Data (GRIB) Stage IV data, version 1.0. UCAR/NCAR Earth Observing Laboratory, accessed 24 September 2021, https://doi.org/10.5065/D6PG1QDD.

Emanuel, K. A., 1986: An air–sea interaction theory for tropical cyclones. Part I: Steady-state maintenance. *J. Atmos. Sci.*, **43**, 585–605, https://doi.org/10.1175/1520-0469(1986)043<0585:AASITF>2.0.CO;2.

——, 1995: Sensitivity of tropical cyclones to surface exchange coefficients and a revised steady-state model incorporating eye dynamics. *J. Atmos. Sci.*, **52**, 3969–3976, https://doi.org/10.1175/1520-0469(1995)052<3969:SOTCTS>2.0.CO;2.

Flather, R. A., 1976: A tidal model of the northwest European continental shelf. *Mem. Soc. Roy. Sci. Liege*, **10**, 141–164.

Fox-Kemper, B., R. Ferrari, and R. Hallberg, 2008: Parameterization of mixed layer eddies. Part I: Theory and diagnosis. *J. Phys. Oceanogr.*, **38**, 1145–1165, https://doi.org/10.1175/2007JPO3792.1.

Gent, P. R., and J. C. McWilliams, 1990: Isopycnal mixing in ocean circulation models. *J. Phys. Oceanogr.*, **20**, 150–155, https://doi.org/10.1175/1520-0485(1990)020<0150:IMIOCM>2.0.CO;2.

——, and Coauthors, 2011: The Community Climate System Model version 4. *J. Climate*, **24**, 4973–4991, https://doi.org/10.1175/2011JCLI4083.1.

Giorgi, F., 2019: Thirty years of regional climate modeling: Where are we and where are we going next? *J. Geophys. Res. Atmos.*, **124**, 5696–5723, https://doi.org/10.1029/2018JD030094.

Green, B. W., and F. Zhang, 2013: Impacts of air–sea flux parameterizations on the intensity and structure of tropical cyclones. *Mon. Wea. Rev.*, **141**, 2308–2324, https://doi.org/10.1175/MWR-D-12-00274.1.

Gutowski, W. J., and Coauthors, 2020: The ongoing need for high-resolution regional climate models: Process understanding and stakeholder information. *Bull. Amer. Meteor. Soc.*, **101**, E664–E683, https://doi.org/10.1175/BAMS-D-19-0113.1.

Haidvogel, D. B., and Coauthors, 2008: Ocean forecasting in terrain-following coordinates: Formulation and skill assessment of the Regional Ocean Modeling System. *J. Comp. Phys.*, **227**, 3595–3624, https://doi.org/10.1016/j.jcp.2007.06.016.

Haus, B. K., D. Jeong, M. A. Donelan, J. A. Zhang, and I. Savelyev, 2010: Relative rates of sea–air heat transfer and frictional drag in very high winds. *Geophys. Res. Lett.*, **37**, L07802, https://doi.org/10.1029/2009GL042206.

Hersbach, H., and Coauthors, 2020: The ERA5 global reanalysis. *Quart. J. Roy. Meteor. Soc.*, **146**, 1999–2049, https://doi.org/10.1002/qj.3803.

Hong, S.-Y., Y. Noh, and J. Dudhia, 2006: A new vertical diffusion package with explicit treatment of entrainment processes. *Mon. Wea. Rev.*, **134**, 2318–2341, https://doi.org/10.1175/MWR3199.1.

Huffman, G. J., and Coauthors, 2007: The TRMM multisatellite precipitation analysis: Quasi-global, multi-year, combined-sensor precipitation estimates at fine scales. *J. Hydrometeor.*, **8**, 38–55, https://doi.org/10.1175/JHM560.1.

Hurrell, J. W., and Coauthors, 2013: The Community Earth System Model: A framework for collaborative research. *Bull. Amer. Meteor. Soc.*, **94**, 1339–1360, https://doi.org/10.1175/BAMS-D-12-00121.1.

Iacono, M. J., J. S. Delamere, E. J. Mlawer, M. W. Shephard, S. A. Clough, and W. D. Collins, 2008: Radiative forcing by long-lived greenhouse gases: Calculations with the AER radiative transfer models. *J. Geophys. Res. Atmos.*, **113**, D13103, https://doi.org/10.1029/2008JD009944.

Jaimes, B., L. K. Shay, and J. K. Brewster, 2016: Observed air–sea interactions in tropical cyclone Isaac over Loop Current mesoscale eddy features. *Dyn. Atmos. Oceans*, **76**, 306–324, https://doi.org/10.1016/j.dynatmoce.2016.03.001.

Jiménez, P. A., J. Dudhia, J. F. González-Rouco, J. Navarro, J. P. Montávez, and E. García-Bustamante, 2012: A revised scheme for the WRF surface layer formulation. *Mon. Wea. Rev.*, **140**, 898–918, https://doi.org/10.1175/MWR-D-11-00056.1.

Unauthenticated | Downloaded 08/28/24 03:34 AM UTC

Kay, J. E., and Coauthors, 2015: The Community Earth System Model (CESM) large ensemble project: A community resource for studying climate change in the presence of internal climate variability. *Bull. Amer. Meteor. Soc.*, **96**, 1333–1349, https://doi.org/10.1175/BAMS-D-13-00255.1.

Kirtman, B. P., and Coauthors, 2012: Impact of ocean model resolution on CCSM climate simulations. *Climate Dyn.*, **39**, 1303–1328, https://doi.org/10.1007/s00382-012-1500-3.

Large, W. G., 2006: Surface fluxes for practitioners of global ocean data assimilation. *Ocean Weather and Forecasting*, E. Chassignet and J. Verron, Eds., Springer, 229–270.

——, and S. Pond, 1981: Open ocean momentum flux measurements in moderate to strong winds. *J. Phys. Oceanogr.*, **11**, 324–336, https://doi.org/10.1175/1520-0485(1981)011<0324:OOMFMI>2.0.CO;2.

——, and ——, 1982: Sensible and latent heat flux measurements over the ocean. *J. Phys. Oceanogr.*, **12**, 464–482, https://doi.org/10.1175/1520-0485(1982)012<0464:SALHFM>2.0.CO;2.

——, and S. G. Yeager, 2004: Diurnal to decadal global forcing for ocean and sea-ice models: The data sets and flux climatologies. NCAR Tech. Note NCAR/TN-460+STR, 112 pp., https://doi.org/10.5065/D6KK98Q6.

——, and ——, 2009: The global climatology of an interannually varying air–sea flux data set. *Climate Dyn.*, **33**, 341–364, https://doi.org/10.1007/s00382-008-0441-3.

——, J. C. McWilliams, and S. C. Doney, 1994: Oceanic vertical mixing: A review and a model with nonlocal boundary layer parameterization. *Rev. Geophys.*, **32**, 363–403, https://doi.org/10.1029/94RG01872.

Lawrence, D. M., and Coauthors, 2011: Parameterization improvements and functional and structural advances in version 4 of the Community Land Model. *J. Adv. Model. Earth Syst.*, **3**, M03001, https://doi.org/10.1029/2011MS000045.

Lemarié, F., J. Kurian, A. F. Shchepetkin, M. J. Molemaker, F. Colas, and J. C. McWilliams, 2012: Are there inescapable issues prohibiting the use of terrain-following coordinates in climate models? *Ocean Modell.*, **42**, 57–79, https://doi.org/10.1016/j.ocemod.2011.11.007.

Li, H., and R. L. Sriver, 2018: Tropical cyclone activity in the high-resolution Community Earth System Model and the impact of ocean coupling. *J. Adv. Model. Earth Syst.*, **10**, 165–186, https://doi.org/10.1002/2017MS001199.

Lin, Y.-L., R. D. Farley, and H. D. Orville, 1983: Bulk parameterization of the snow field in a cloud model. *J. Climate Appl. Meteor.*, **22**, 1065–1092, https://doi.org/10.1175/1520-0450(1983)022<1065:BPOTSF>2.0.CO;2.

Ma, X., and Coauthors, 2016: Western boundary currents regulated by interaction between ocean eddies and the atmosphere. *Nature*, **535**, 533–537, https://doi.org/10.1038/nature18640.

Maslowski, W., J. C. Kinney, M. Higgins, and A. Roberts, 2012: The future of Arctic sea ice. *Annu. Rev. Earth Planet. Sci.*, **40**, 625–654, https://doi.org/10.1146/annurev-earth-042711-105345.

McWilliams, J. C., 2016: Submesoscale currents in the ocean. *Proc. Roy. Soc. London*, **472A**, 20160117, https://doi.org/10.1098/rspa.2016.0117.

Monin, A. S., and A. M. F. Obukhov, 1954: Basic laws of turbulent mixing in the surface layer of the atmosphere. *Tr. Akad. Nauk. SSSR Geophiz. Inst.*, **24**, 163–187.

Muller-Karger, F. E., and Coauthors, 2015: Natural variability of surface oceanographic conditions in the offshore Gulf of Mexico. *Prog. Oceanogr.*, **134**, 54–76, https://doi.org/10.1016/j.pocean.2014.12.007.

Oey, L. Y., T. Ezer, and H.-C. Lee, 2005: Loop current, rings and related circulation in the Gulf of Mexico: A review of numerical models and future challenges. Circulation in the Gulf of Mexico: Observations and Models, *Geophys. Monogr*., Vol. 161, Amer. Geophys. Union, 31–56.

Oleson, K., G. Bonan, J. Feddema, M. Vertenstein, and E. Kluzek, 2010a: Technical description of an urban parameterization for the Community Land Model (CLMU). NCAR Tech. Note NCAR/TN-480+STR, 169 pp., https://doi.org/10.5065/D6K35RM9.

——, and Coauthors, 2010b: Technical description of version 4.0 of the Community Land Model (CLM). NCAR Tech. Note NCAR/TN-478+STR, 257 pp., https://doi.org/10.5065/D6FB50WZ.

Otto-Bliesner, B. L., and Coauthors, 2016: Climate variability and change since 850 CE: An ensemble approach with the Community Earth System Model. *Bull. Amer. Meteor. Soc.*, **97**, 735–754, https://doi.org/10.1175/BAMS-D-14-00233.1.

Pleim, J. E., and A. Xiu, 1995: Development and testing of a surface flux and planetary boundary layer model for application in mesoscale models. *J. Appl. Meteor.*, **34**, 16–32, https://doi.org/10.1175/1520-0450-34.1.16.

Putrasahan, D. A., A. J. Miller, and H. Seo, 2013: Isolating mesoscale coupled ocean–atmosphere interactions in the Kuroshio Extension region. *Dyn. Atmos. Oceans*, **63**, 60–78, https://doi.org/10.1016/j.dynatmoce.2013.04.001.

Reed, K. A., J. T. Bacmeister, N. A. Rosenbloom, M. F. Wehner, S. C. Bates, P. H. Lauritzen, J. E. Truesdale, and C. Hannay, 2015: Impact of the dynamical core on the direct simulation of tropical cyclones in a high-resolution global model. *Geophys. Res. Lett.*, **42**, 3603–3608, https://doi.org/10.1002/2015GL063974.

Renault, L., J. C. McWilliams, and J. Gula, 2018: Dampening of submesoscale currents by air–sea stress coupling in the Californian upwelling system. *Sci. Rep.*, **8**, 132388, https://doi.org/10.1038/s41598-018-31602-3.

——, S. Masson, V. Oerder, S. Jullien, and F. Colas, 2019: Disentangling the mesoscale ocean-atmosphere interactions. *J. Geophys. Res. Oceans*, **124**, 2164–2178, https://doi.org/10.1029/2018JC014628.

Richter, D. H., R. Bohac, and D. P. Stern, 2016: An assessment of the flux profile method for determining air–sea momentum and enthalpy fluxes from dropsonde data in tropical cyclones. *J. Atmos. Sci.*, **73**, 2665–2682, https://doi.org/10.1175/JAS-D-15-0331.1.

Roberts, M. J., and Coauthors, 2020: Projected future changes in tropical cyclones using the CMIP6 HighResMIP multimodel ensemble. *Geophys. Res. Lett.*, **47**, e2020GL088662, https://doi.org/10.1029/2020GL088662.

Saha, S., and Coauthors, 2010: The NCEP Climate Forecast System Reanalysis. *Bull. Amer. Meteor. Soc.*, **91**, 1015–1058, https://doi.org/10.1175/2010BAMS3001.1.

——, and Coauthors, 2014: The NCEP Climate Forecast System version 2. *J. Climate*, **27**, 2185–2208, https://doi.org/10.1175/JCLI-D-12-00823.1.

Samson, G., S. Masson, F. Durand, P. Terray, S. Berthet, and S. Jullien, 2017: Roles of land surface albedo and horizontal resolution on the Indian summer monsoon biases in a coupled ocean–atmosphere tropical-channel model. *Climate Dyn.*, **48**, 1571–1594, https://doi.org/10.1007/s00382-016-3161-0.

Sanford, T. B., J. F. Price, J. B. Girton, and D. C. Webb, 2007: Highly resolved observations and simulations of the ocean response to a hurricane. *Geophys. Res. Lett.*, **34**, L13604, https://doi.org/10.1029/2007GL029679.

Schneider, N., and B. Qiu, 2015: The atmospheric response to weak sea surface temperature fronts. *J. Atmos. Sci.*, **72**, 3356–3377, https://doi.org/10.1175/JAS-D-14-0212.1.

Seo, H., A. J. Miller, and J. O. Roads, 2007: The Scripps Coupled Ocean-Atmosphere Regional (SCOAR) model, with applications in the eastern Pacific sector. *J. Climate*, **20**, 381–402, https://doi.org/10.1175/JCLI4016.1.

Shchepetkin, A. F., and J. C. McWilliams, 2005: The Regional Oceanic Modeling System (ROMS): A split-explicit, free-surface, topography-following-coordinate oceanic model. *Ocean Modell.*, **9**, 347–404, https://doi.org/10.1016/j.ocemod.2004.08.002.

——, and ——, 2009: Correction and commentary for "ocean forecasting in terrain-following coordinates: Formulation and skill assessment of the regional ocean modelling system" by Haidvogel et al. J. Comput. Phys., 227, pp. 3595–3624. *J. Comput. Phys.*, **228**, 8985–9000, https://doi.org/10.1016/j.jcp.2009.09.002.

Shutts, G. J., 2005: A kinetic energy backscatter algorithm for use in ensemble prediction systems. *Quart. J. Roy. Meteor. Soc.*, **131**, 3079–3102, https://doi.org/10.1256/qj.04.106.

Skamarock, W. C., and Coauthors, 2008: A description of the Advanced Research WRF version 3. NCAR Tech. Note NCAR/TN-475+STR, 113 pp., https://doi.org/10.5065/D68S4MVH.

Small, R. J., and Coauthors, 2008: Air–sea interaction over ocean fronts and eddies. *Dyn. Atmos. Oceans*, **45**, 274–319, https://doi.org/10.1016/j.dynatmoce.2008.01.001.

——, and Coauthors, 2014: A new synoptic scale resolving global climate simulation using the Community Earth System Model. *J. Adv. Model. Earth Syst.*, **6**, 1065–1094, https://doi.org/10.1002/2014MS000363.

Unauthenticated | Downloaded 05/28/24 03:34 AM UTC

Smith, T. A., S. Chen, T. Campbell, E. Rogers, S. Gabersek, D. Wang, S. Carroll, and R. Allard, 2013: Ocean–wave coupled modeling in COAMPS-TC: A study of Hurricane Ivan (2004). *Ocean Dyn.*, **69**, 181–194, https://doi.org/10.1016/j.ocemod.2013.06.003.

Song, Q., D. Chelton, S. Esbensen, N. Thum, and L. O'Neill, 2009: Coupling between sea surface temperature and low-level winds in mesoscale numerical models. *J. Climate*, **22**, 146–164, https://doi.org/10.1175/2008JCLI2488.1.

Thomas, L., A. Tandon, and A. Mahadevan, 2008: Submesoscale ocean processes and dynamics. Ocean Modeling in an Eddying Regime, *Geophys. Monogr*., Vol. 177, Amer. Geophys. Union, 217–228.

Warner, J. C., B. Armstrong, R. He, and J. B. Zambon, 2010: Development of a Coupled Ocean-Atmosphere-Wave-Sediment Transport (COAWST) modeling system. *Ocean Modell.*, **35**, 230–244, https://doi.org/10.1016/j.ocemod.2010.07.010.

Wehner, M. F., and Coauthors, 2014: The effect of horizontal resolution on simulation quality in the Community Atmospheric Model, CAM5.1. *J. Adv. Model. Earth Syst.*, **6**, 980–997, https://doi.org/10.1002/2013MS000276.

Xie, S.-P., and Coauthors, 2007: A regional ocean–atmosphere model for eastern Pacific climate: Towards reducing tropical biases. *J. Climate*, **20**, 1504–1522, https://doi.org/10.1175/JCLI4080.1.

Zarzycki, C. M., and C. Jablonowski, 2014: A multi-decadal simulation of Atlantic tropical cyclones using a variable-resolution global atmospheric general circulation model. *J. Adv. Model. Earth Syst.*, **6**, 805–828, https://doi.org/10.1002/2014MS000352.

——, K. A. Reed, J. T. Bacmeister, A. P. Craig, S. C. Bates, and N. A. Rosenbloom, 2016: Impact of surface coupling grids on tropical cyclone extremes in high-resolution atmospheric simulations. *Geosci. Model Dev.*, **9**, 779–788, https://doi.org/10.5194/gmd-9-779-2016.

Zhang, D.-L., and R. A. Anthes, 1982: A high-resolution model of the planetary boundary layer—Sensitivity tests and comparisons with SESAME-79 data. *J. Appl. Meteor.*, **21**, 1594–1609, https://doi.org/10.1175/1520-0450(1982)021<1594:AHRMOT>2.0.CO;2.

Zhang, J. A., P. G. Black, J. R. French, and W. M. Drennan, 2008: First direct measurements of enthalpy flux in the hurricane boundary layer: The CBLAST results. *Geophys. Res. Lett.*, **35**, L14813, https://doi.org/10.1029/2008GL034374.

Zhang, S., M. J. Harrison, A. T. Wittenberg, A. Rosati, J. L. Anderson, and V. Balaji, 2005: Initialization of an ENSO forecast system using a parallelized ensemble filter. *Mon. Wea. Rev.*, **133**, 3176–3201, https://doi.org/10.1175/MWR3024.1.

——, ——, A. Rosati, and A. Wittenberg, 2007: System design and evaluation of coupled ensemble data assimilation for global oceanic climate studies. *Mon. Wea. Rev.*, **135**, 3541–3564, https://doi.org/10.1175/MWR3466.1.

Zhao, L., and Coauthors, 2021: Global multi-model projections of local urban climates. *Nat. Climate Change*, **11**, 152–157, https://doi.org/10.1038/s41558-020-00958-8.

Unauthenticated | Downloaded 05/28/24 03:34 AM UTC